Scaling laws for unsteady natural convection cooling of fluid with Prandtl number less than one in a vertical cylinder

Wenxian Lin[1,2,*] and S. W. Armfield[2]

[1]*Solar Energy Research Institute, Yunnan Normal University, Kunming, Yunnan 650092, People's Republic of China*
[2]*School of Aerospace, Mechanical and Mechatronic Engineering, University of Sydney, New South Wales 2006, Australia*

The flow behavior associated with cooling an initially quiescent isothermal Newtonian fluid with Prandtl number (Pr) less than one in a vertical cylinder by unsteady natural convection with an imposed lower temperature on vertical sidewalls is investigated by scaling analysis and direct numerical simulation. The flow is dominated by three distinct stages of development, i.e., the boundary-layer development stage adjacent to the sidewall, the stratification stage, and the cooling-down stage, respectively. The first stage can be further divided into three distinct substages, i.e., the start-up stage, the transitional stage, and the boundary-layer steady-state stage, respectively. A scaling analysis is carried out to obtain scaling laws for the basic flow features in terms of the flow control parameters, i.e., the Rayleigh number Ra, Pr, and the aspect ratio of the cylinder A, respectively. A series of direct numerical simulations with selected values of A, Ra, and Pr in the ranges of $1/3 \leq A \leq 3$, $10^6 \leq \mathrm{Ra} \leq 10^{10}$, and $0.01 \leq \mathrm{Pr} \leq 0.5$ are carried out, and it is found that the numerical results agree well with the scaling laws. These numerical results are further used to quantify these scaling laws for Ra, A, and Pr in the above-mentioned ranges.

I. INTRODUCTION

Determining the behavior of a fluid in a cylinder cooled or heated by the imposition of a constant temperature, different from the fluid temperature, or heat flux, on the container wall is an important engineering problem. This flow has many features in common with the differentially heated sidewall flow which has been studied extensively (see, e.g., Refs. [1,2]). In this paper similar techniques will be used to examine the cooling down flow.

Scaling analysis is a very effective and easy-to-use tool for some nonlinear physical phenomena [3]. Patterson and Imberger [4] used a scaling analysis in their pioneering investigation of the transient behavior that occurs when the opposing two vertical sidewalls of a two-dimensional rectangular cavity are impulsively heated and cooled by an equal amount. They devised a classification of the flow development through several transient flow regimes to one of three steady-state types of flow based on the relative values of the dimensionless Rayleigh number Ra, Prandtl number Pr, and aspect ratio of cavity A. This Patterson-Imberger flow model has since occupied the center stage of research into understanding natural convection flow in cavities, and numerous investigations subsequently focused on diverse aspects of the model [5–13].

More recently, the authors carried out scaling analysis and direct numerical simulation of the transient processes of cooling an initially homogeneous fluid with $\mathrm{Pr} \geq 1$ by natural convection in a vertical circular cylinder and in a rectangular container [14,15]. The results show that vigorous flow activities are concentrated mainly in the vertical thermal boundary

layer along the sidewall and in the horizontal region comprising the lower part of the domain where the cold intrusion flow is created. The transient flow patterns at the unsteady and quasi-steady-state stages were analyzed, including the activities of the traveling waves in the vertical thermal boundary layer along the sidewall, the cold intrusion movements in the horizontal region, the stratification of the fluid, and the long-term behavior beyond the full stratification. Various scaling laws characterizing the flow evolution at these distinct development stages were developed by scaling analyses, which were then verified and quantified by extensive direct numerical simulations under different flow situations in terms of Ra, Pr, and A. Lin, Armfield, and Morgan [16] also obtained the scaling laws for the boundary-layer development along a vertical isothermal plate in a linearly stratified fluid with $\mathrm{Pr} > 1$. Oliveski, Krenzinger, and Vielmo [17] made a numerical and an experimental analysis of velocity and temperature fields inside a storage tank subjected to natural convection cooling, while Kwak, Kuwahara, and Hyun [18] conducted a numerical study on the transient natural convective cool-down process of a fluid in a cylindrical container, with emphasis on the flow patterns when the maximum density temperature is experienced.

The majority of the past studies have focused on fluids with $\mathrm{Pr} \geq 1$ owing to their relevance in theoretical and practical applications. Natural convection flows with $\mathrm{Pr} < 1$ are very important as well, in such applications as the Earth's liquid core convection, crystal growth in semiconductors, melting processes, etc., not to mention those using air and other gases as the working medium. However, studies on unsteady natural convection flows of fluids with $\mathrm{Pr} \leq 1$ resulting from heating/cooling vertical boundaries, together with studies on the effect of Pr variation, are scarce. This scarcity can be further illustrated, as an example, by the seemingly contradictory statements made in the celebrated

---

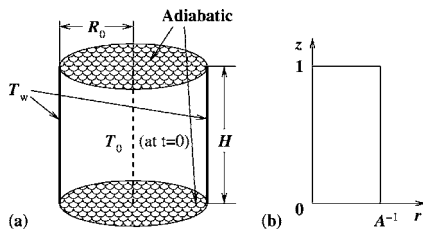*Corresponding author. Electronic address: wenxian.lin@aeromech.usyd.edu.au

FIG. 1. A sketch of (a) the physical system considered and (b) the appropriate computational domain used for numerical simulations.

books of Incropera and DeWitt [19], Tritton [20], and Gebhart *et al.* [21], where it was stated in the first two books that the viscous boundary layer should be much thinner than the thermal boundary layer when $Pr \ll 1$ whereas in the third book it was argued that both boundary layers should have approximately the same thickness for $Pr < 1$, even for Pr as small as 0.01. This scarcity, together with the apparently incomplete understanding of $Pr \lesssim 1$ flows, motivates the current study.

In this study, the behavior of cooling a quiescent isothermal Newtonian fluid with $Pr < 1$ in a vertical cylinder by unsteady natural convection with an imposed lower temperature on vertical sidewalls is investigated by scaling analysis and direct numerical simulation. The scaling analysis is carried out in Sec. II to develop scaling laws for the parameters characterizing the flow behavior at different stages of flow development. These scaling laws are then validated and quantified in Sec. III by a series of direct numerical simulations with selected values of A, Ra, and Pr in the ranges of $1/3 \leq A \leq 3$, $10^6 \leq Ra \leq 10^{10}$, and $0.01 \leq Pr \leq 0.5$. Finally, some discussions and conclusions are carried out in Sec. IV.

II. SCALING ANALYSIS

Under consideration is the flow behavior of cooling a quiescent isothermal Newtonian fluid with $Pr < 1$ in a vertical cylinder by unsteady natural convection due to an imposed fixed lower temperature on the vertical sidewalls. The physical system considered in this study and the appropriate computational domain used for numerical simulations are schematically depicted in Fig. 1. The cylinder has a height of H (m) and a radius of R_0 (m). It is assumed that the fluid cooling is the result of the imposed fixed temperature T_w (°C) on the vertical sidewalls while all the remaining boundaries are adiabatic and all boundaries are nonslip, and the fluid in the cylinder is initially at rest and at a uniform temperature T_0 (°C, $T_0 > T_w$).

It is hypothesized that the flow considered here is dominated by three distinct stages of development, similar to those with $Pr \geq 1$ [14,15], i.e., the boundary-layer development stage, the stratification stage, and the cooling-down stage, respectively. The flow development is illustrated in Fig. 2, where numerically simulated temperature contours are shown for the three stages for the specific case of Ra $=10^8$, Pr=0.1, and $A=1$, where Ra, Pr, and A are defined as

$$Ra = \frac{g\beta(T_0 - T_w)H^3}{\nu\kappa}, \quad Pr = \frac{\nu}{\kappa}, \quad A = \frac{H}{R_0},$$

in which g is the acceleration due to gravity (m s^{-2}); β, ν, and κ are the thermal expansion coefficient (K^{-1}), kinematic
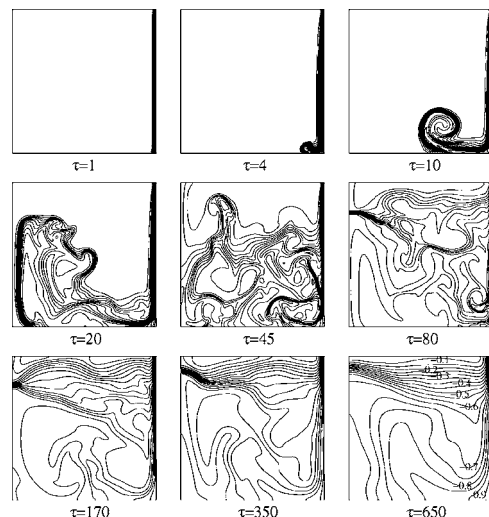

FIG. 2. Numerically simulated temperature contours at the stages of the boundary-layer development (top row), the stratification (middle row), and the cooling down (bottom row), respectively, for $Ra=10^8$, $A=1$, and Pr=0.1. τ is made dimensionless by $H^2/(\kappa Ra^{1/2})$.

viscosity (m^2 s^{-1}), and thermal diffusivity (m^2 s^{-1}) of the fluid, respectively. It is noted here that this Ra is based on the flow properties at time $t=0$. An instantaneous Ra based on the developing flow would be less, as the boundary-layer height and temperature difference reduce with time. In this case the boundary-layer development is seen in the temperature contours adjacent to the right-hand, cooled, wall, with the boundary-layer development completed by around $\tau = 10$, where τ is the dimensionless time, made dimensionless by $H^2/(\kappa Ra^{1/2})$. The cooled fluid ejected by the boundary layer acts to fill and stratify the domain, seen in the stratification stage, from $\tau=20$ to 80. Finally the stratification is gradually reduced in the cooling-down stage of the flow, for $\tau > 170$.

Previous studies dealing with natural convection flows have demonstrated that three-dimensional effects can occur in natural convection boundary layers at Rayleigh numbers comparable to the upper range considered here [22,23]. The time scale for the growth of the three-dimensional structures has been shown to be large with respect to the time scale of the boundary layer growth [24] and it is therefore considered unlikely that three-dimensional structures would be observed in the boundary layer growth stage for the flow considered here. In the stratification and final cooling down stages of the flow the instantaneous Rayleigh number is steadily dropping, as a result of reduction in the boundary layer height and in the temperature difference and the long-term behavior is therefore also considered unlikely to be three-dimensional. Further, it is noted by Juel *et al.* [23] that where three-dimensional structures were observed for very small Pr (Pr =0.025) in a small-aspect-ratio rectangular, differentially heated enclosure, the associated velocities were an order of magnitude less than the two-dimensional velocities and had no significant effect on the heat transfer rates. It is therefore assumed that the flows are laminar and axisymmetric and the computational domain shown in Fig. 1(b) is appropriate.

The governing equations of motion are the Navier-Stokes equations with the Boussinesq approximation for buoyancy, which together with the temperature transport equation can be written in the following two-dimensional form,

$$\frac{1}{R}\frac{\partial(RU)}{\partial R} + \frac{\partial V}{\partial Z} = 0, \tag{1}$$

$$\frac{\partial U}{\partial t} + \frac{1}{R}\frac{\partial(RUU)}{\partial R} + \frac{\partial(VU)}{\partial Z}$$
$$= -\frac{1}{\rho}\frac{\partial P}{\partial R} + \nu\left[\frac{\partial}{\partial R}\left(\frac{1}{R}\frac{\partial(RU)}{\partial R}\right) + \frac{\partial^2 U}{\partial Z^2}\right], \tag{2}$$

$$\frac{\partial V}{\partial t} + \frac{1}{R}\frac{\partial(RUV)}{\partial R} + \frac{\partial(VV)}{\partial Z}$$
$$= -\frac{1}{\rho}\frac{\partial P}{\partial Z} + \nu\left[\frac{1}{R}\frac{\partial}{\partial R}\left(R\frac{\partial V}{\partial R}\right) + \frac{\partial^2 V}{\partial Z^2}\right] + g\beta(T - T_0), \tag{3}$$

$$\frac{\partial T}{\partial t} + \frac{1}{R}\frac{\partial(RUT)}{\partial R} + \frac{\partial(VT)}{\partial Z} = \kappa\left[\frac{1}{R}\frac{\partial}{\partial R}\left(R\frac{\partial T}{\partial R}\right) + \frac{\partial^2 T}{\partial Z^2}\right], \tag{4}$$

where U and V are the radial (R direction) and vertical (Z direction) velocity components (m s^{-1}), t is the time (s), P is the pressure (Pa), T is the temperature (°C), and ρ is the density of fluid (kg m^{-3}), respectively. The gravity acts in the negative Z direction.

In this section, scaling laws will be developed for the relevant parameters characterizing the flow behavior at these respective stages of flow development. As there are, to our best knowledge, no suitable experimental results to validate these scaling laws, they are then validated and quantified in Sec. III by a series of direct numerical simulations with selected values of A, Ra, and Pr in the ranges of $1/3 \leqslant A \leqslant 3$, $10^6 \leqslant \text{Ra} \leqslant 10^{10}$, and $0.01 \leqslant \text{Pr} \leqslant 0.5$.

A. Boundary-layer development stage

After the initiation of the flow, a vertical boundary layer will be developed adjacent to the cooled sidewall and will experience a start-up stage, followed by a short transitional stage before reaching a steady-state stage. The parameters characterizing the flow behavior at the boundary-layer development stage are predominantly the thermal boundary-layer thickness Δ_T (m), the maximum vertical velocity V_m (m s^{-1}) within the boundary layer, the time t_s (s) for the boundary-layer development to reach the steady state, and the Nusselt number Nu (dimensionless) across the sidewall, respectively, as illustrated in Fig. 3, where the numerically simulated typical time series of δ_T ($\delta_T = \Delta_T/H$, dimensionless), v_m [$v_m = V_m H/(\kappa \text{Ra}^{1/2})$, dimensionless], and the local Nusselt number Nu at the height of $Z=0.5H$ as well as the average Nusselt number $\overline{\text{Nu}}$ (dimensionless) over the whole sidewall are presented. The thermal boundary-layer thickness Δ_T is defined as the radial distance between the location where the fluid temperature reaches $0.01(T_w - T_0)$ and the sidewall. Nu
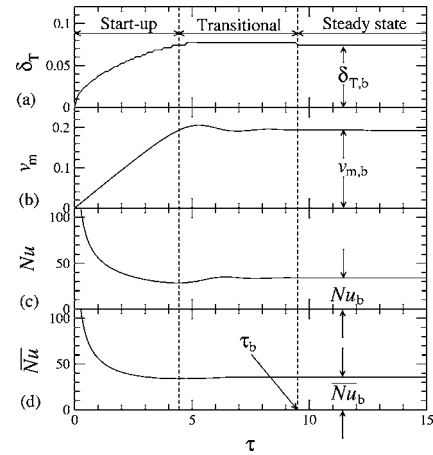

FIG. 3. A definition of the three distinct substages at the boundary-layer development stage and the numerically simulated typical time series of (a) the local thermal boundary-layer thickness δ_T ($\delta_T = \Delta_T/H$) at the height of $Z=0.5H$; (b) the local maximum vertical velocity v_m ($v_m = V_m[H/(\kappa \text{Ra}^{1/2})]$) within the boundary layer at the height of $Z=0.5H$; (c) the local Nusselt number Nu at the height of $Z=0.5H$; and (d) the average Nusselt number $\overline{\text{Nu}}$ over the vertical sidewall, respectively, for the specific case of Ra$=10^8$, Pr$=0.1$, and $A=1$. τ is made dimensionless by $H^2/(\kappa \text{Ra}^{1/2})$.

and $\overline{\text{Nu}}$ will be defined below in Eq. (14). The time τ_b for the boundary-layer development to reach the steady state, which is made dimensionless by $H^2/(\kappa \text{Ra}^{1/2})$, is determined as the moment when Δ_T ceases to change with time [the criterion for the determination of τ_b used in the subsequent numerical simulations is when the difference between $\Delta_T(\tau_b)$ and its value at the previous time-step is within 0.01%].

Scalings for these quantities may be developed following Patterson and Imberger [4] as follows. Heat is initially transferred out through the vertical wall from the fluid by conduction after the initiation of the flow, resulting in a vertical thermal boundary layer of thickness $O(\Delta_T)$ adjacent to the wall, where at height Z, from Eq. (4), the balance between the inertial term $O((T_0 - T_w)/t)$ and the conductive term $O(\kappa(T_0 - T_w)/\Delta_T^2)$ dominates the flow, which gives

$$\Delta_T \sim \kappa^{1/2} t^{1/2}, \tag{5}$$

where "$\sim$" means "scales with," which was also obtained by Patterson and Imberger [4] for the Pr>1 case.

During this start-up stage, in contrast to the case of Pr >1, the dominant balance in Eq. (3) for Pr<1 is that between the inertia force $O(V_m/t)$ and the buoyant force $O(g\beta(T_0 - T_w))$, which gives

$$V_m \sim g\beta(T_0 - T_w)t \sim \frac{\text{Ra}\nu\kappa}{H^3}t. \tag{6}$$

After the start-up stage, the dominant balance at height Z in Eq. (4) gradually shifts from that between the inertial term $O((T_0 - T_w)/t)$ and the conductive term $O(\kappa(T_0 - T_w)/\Delta_T^2)$ to that between the inertial term and the convective term $O(V_m(T_0 - T_w)/(H - Z))$, represented by a transitional stage as illustrated in Fig. 3, until the latter balance becomes fully

dominant and the thermal boundary-layer development then reaches its steady-state stage.

The inertia-convective balance in Eq. (4) gives

$$\frac{T_0 - T_w}{t} \sim \frac{V_m(T_0 - T_w)}{H - Z}. \tag{7}$$

Using Eqs. (5) and (6), this leads to

$$t_b \sim \left(\frac{H - Z}{g\beta(T_0 - T_w)}\right)^{1/2} \sim \frac{H^2}{\kappa \mathrm{Ra}^{1/2}\mathrm{Pr}^{1/2}}\left(1 - \frac{Z}{H}\right)^{1/2}, \tag{8}$$

which represents the local time scale (s) for the thermal boundary layer at height Z to reach the steady state. Therefore, the scaling law for the maximum time scale $t_{b,m}$ (s) within the boundary layer, which is at $Z=0$, is as follows:

$$t_{b,m} \sim \left(\frac{H}{g\beta(T_0 - T_w)}\right)^{1/2} \sim \frac{H^2}{\kappa \mathrm{Ra}^{1/2}\mathrm{Pr}^{1/2}}. \tag{9}$$

At time t_b, the thermal boundary layer at height Z reaches its steady-state thickness scale $\Delta_{T,b}$ (m), which, from Eq. (5), is as follows,

$$\Delta_{T,b} \sim \kappa^{1/2}\left(\frac{H - Z}{g\beta(T_0 - T_w)}\right)^{1/4} \sim \frac{H^{3/4}(H - Z)^{1/4}}{\mathrm{Ra}^{1/4}\mathrm{Pr}^{1/4}}, \tag{10}$$

and the steady-state vertical velocity scale $V_{m,b}(\mathrm{m\ s}^{-1})$ at height Z within this thermal boundary layer is, from Eq. (6), as follows,

$$V_{m,b} \sim [(H - Z)g\beta(T_0 - T_w)]^{1/2} \sim \frac{\kappa \mathrm{Ra}^{1/2}\mathrm{Pr}^{1/2}}{H}\left(1 - \frac{Z}{H}\right)^{1/2}. \tag{11}$$

A scaling for the viscous boundary-layer thickness may be developed in a manner analogous to that of $\Delta_{T,b}$, but with $\Delta_v \sim \nu^{1/2}t^{1/2}$ (m) at the start-up stage. This will give

$$\Delta_{v,b,1} \sim \Delta_{T,b}\mathrm{Pr}^{1/2}, \tag{12}$$

indicating that for $\mathrm{Pr}<1$ the region over which the balance between vertical acceleration and viscous diffusion of momentum, that is the near wall region, is smaller than for the corresponding thermal conduction region. The vertical velocity boundary layer therefore comprises two regions: a near wall inner region governed by the wall conditions given by Eq. (12), and an outer region in which the flow is governed by a balance between vertical acceleration and buoyancy determined by the extent of thermal boundary layer, that is

$$\Delta_{v,b,2} \approx \Delta_{T,b}. \tag{13}$$

This two-region boundary layer is consistent with the comments by Incropera and DeWitt [19], Tritton [20], and Gebhart et al. [21]. It should be noted that Eq. (12) was also obtained by Patterson and Imberger [4] for the $\mathrm{Pr}>1$ case, indicating that the vertical velocity boundary layer is embedded within the thermal boundary layer and is governed exclusively by the single balance between vertical acceleration and viscous diffusion of momentum.

The heat transfer across the vertical sidewall is represented by the local Nusselt number Nu at height Z and the average Nusselt number $\overline{\mathrm{Nu}}$ over the whole sidewall, which are defined respectively as follows,

$$\mathrm{Nu} \sim \left(\frac{R_0}{(T_0 - T_w)}\frac{\partial T}{\partial R}\right)_{R=R_0}, \quad \overline{\mathrm{Nu}} = \frac{1}{H}\int_0^H \mathrm{Nu}\,dZ. \tag{14}$$

Therefore, during the start-up stage,

$$\mathrm{Nu} \sim \frac{R_0}{\Delta_T} \sim \frac{R_0}{\kappa^{1/2}t^{1/2}}, \tag{15}$$

$$\overline{\mathrm{Nu}} \sim \frac{1}{H}\int_0^H \frac{R_0}{\Delta_T}dZ \sim \frac{R_0}{\kappa^{1/2}t^{1/2}}, \tag{16}$$

and at the steady-state stage,

$$\mathrm{Nu}_b \sim \frac{R_0}{\Delta_{T,b}} \sim \frac{(\mathrm{PrRa})^{1/4}}{A(1 - Z/H)^{1/4}}, \tag{17}$$

$$\overline{\mathrm{Nu}}_b \sim \frac{1}{H}\int_0^H \frac{R_0}{\Delta_{T,b}}dZ \sim \frac{(\mathrm{PrRa})^{1/4}}{A}. \tag{18}$$

B. Stratification stage

Once the boundary layer is fully developed, the fluid in the cylinder is gradually stratified by the cooled fluid ejected from the boundary layer, starting from the bottom of the cylinder. The time t_s (s) for the full stratification of the whole fluid in the cylinder will be at the moment when the volume of the cooled fluid ejected from the boundary layer is equal to the volume of the cylinder. The rate of flow of fluid through the boundary layer is characterized by $\Delta_{T,b}V_{m,b}$, and therefore the time to full stratification is characterized by

$$t_s \sim \frac{HR_0}{\kappa \mathrm{Ra}^{1/2}}\left(\frac{\mathrm{Ra}}{\mathrm{Pr}}\right)^{1/4}. \tag{19}$$

C. Cooling-down stage

After the full stratification, the fluid in the cylinder is continually cooled down until the whole body of fluid has the same temperature as that imposed on the sidewalls. The appropriate parameters to characterize this cooling-down process are the time t_f (s) for the fluid to be fully cooled down, the average fluid temperature $T_a(t)$ (°C) over the whole volume of the cylinder at time t, and the average Nusselt number on the cooling wall.

As the fluid cooling down is achieved by maintaining a fixed temperature T_w on the vertical sidewalls while keeping the top and bottom boundaries adiabatic, all the heat used to fully cool down the fluid in the cylinder must pass through the sidewalls, and then energy conservation in the cylinder requires that

$$\rho c_p V_c (T_0 - T_w) \sim t_f A_s k \frac{(T_0 - T_w)}{\bar{\Delta}_{T,b}}, \qquad (20)$$

where $V_c = \pi R_0^2 H$ (m³) is the volume of the fluid in the cylinder, $A_s = 2\pi R_0 H$ (m²) is the surface area of the sidewall, k (W mK⁻¹) is the thermal conductivity of fluid, and $\bar{\Delta}_{T,b}$ (m) is the average thermal boundary-layer thickness, which is calculated as follows,

$$\bar{\Delta}_{T,b} = \frac{1}{H} \int_0^H \Delta_{T,b} dZ. \qquad (21)$$

Therefore, t_f has the following scaling law,

$$t_f \sim \frac{R_0 \bar{\Delta}_{T,b}}{\kappa} \sim \frac{R_0 H}{\kappa (\mathrm{PrRa})^{1/4}}, \qquad (22)$$

where $\kappa = k/(\rho c_p)$.

The decay of the average fluid temperature $T_a(t)$ is expected to obey an exponential relation [25], that is,

$$\frac{T_a(t) - T_0}{T_0 - T_w} = e^{-f(\mathrm{Ra},\mathrm{Pr},A)t} - 1, \qquad (23)$$

where $f(\mathrm{Ra},\mathrm{Pr},A)$ is some function of Ra, Pr, and A. If t_f is defined as the time when $T_a(t_f) - T_0 = 0.99(T_w - T_0)$, then $f(\mathrm{Ra},\mathrm{Pr},A)$ will have the following form,

$$f(\mathrm{Ra},\mathrm{Pr},A) \sim \frac{1}{t_f}. \qquad (24)$$

III. NUMERICAL RESULTS

In this section, the scaling laws obtained above will be validated and quantified by a series of direct numerical simulations with selected values of A, Ra, and Pr in the ranges of $1/3 \le A \le 3$, $10^6 \le \mathrm{Ra} \le 10^{10}$, and $0.01 \le \mathrm{Pr} \le 0.5$. A total of 12 simulation runs have been carried out for this purpose. Specifically, results have been obtained with $\mathrm{Ra} = 10^6$, 10^7, 10^8, 10^9, and 10^{10}, while keeping $A = 1$ and $\mathrm{Pr} = 0.1$ unchanged, to show the dependence of the scaling laws on Ra (Runs 1–5); the runs with $A = 1/3$, $1/2$, 1, 2, and 3, while keeping $\mathrm{Ra} = 10^8$ and $\mathrm{Pr} = 0.1$ unchanged, have been carried out to show the dependence on A (Runs 6–7, 3, and 8–9); and the runs with $\mathrm{Pr} = 0.01$, 0.05, 0.1, and 0.5, while keeping $\mathrm{Ra} = 10^8$ and $A = 1$ unchanged, have been carried out to show the dependence on Pr (Runs 10–11, 3, and 12), respectively.

A. Governing equations, initial and boundary conditions, and scaling laws in dimensionless form

The governing equations (1)–(4) can be expressed in the following dimensionless forms,

$$\frac{1}{r} \frac{\partial(ru)}{\partial r} + \frac{\partial v}{\partial z} = 0, \qquad (25)$$

$$\frac{\partial u}{\partial \tau} + \frac{1}{r} \frac{\partial(ruu)}{\partial r} + \frac{\partial(vu)}{\partial z}$$
$$= -\frac{\partial p}{\partial r} + \frac{\mathrm{Pr}}{\mathrm{Ra}^{1/2}} \left[\frac{\partial}{\partial r} \left(\frac{1}{r} \frac{\partial(ru)}{\partial r} \right) + \frac{\partial^2 u}{\partial z^2} \right], \qquad (26)$$

$$\frac{\partial v}{\partial \tau} + \frac{1}{r} \frac{\partial(ruv)}{\partial r} + \frac{\partial(vv)}{\partial z} = -\frac{\partial p}{\partial z} + \frac{\mathrm{Pr}}{\mathrm{Ra}^{1/2}} \left[\frac{1}{r} \frac{\partial}{\partial r} \left(r \frac{\partial v}{\partial r} \right) + \frac{\partial^2 v}{\partial z^2} \right]$$
$$+ \mathrm{Pr}\theta, \qquad (27)$$

$$\frac{\partial \theta}{\partial \tau} + \frac{1}{r} \frac{\partial(ru\theta)}{\partial r} + \frac{\partial(v\theta)}{\partial z} = \frac{1}{\mathrm{Ra}^{1/2}} \left[\frac{1}{r} \frac{\partial}{\partial r} \left(r \frac{\partial \theta}{\partial r} \right) + \frac{\partial^2 \theta}{\partial z^2} \right] \qquad (28)$$

where r, z, u, v, τ, p, and θ are respectively the dimensionless forms of R, Z, U, V, t, P, and T, which are made dimensionless by

$$r = \frac{R}{H}, \quad z = \frac{Z}{H}, \quad u = \frac{U}{V_0}, \quad v = \frac{V}{V_0}, \quad \tau = \frac{t}{(H/V_0)},$$

$$p = \frac{P}{\rho V_0^2}, \quad \theta = \frac{T - T_0}{T_0 - T_w},$$

where $V_0 = \kappa \mathrm{Ra}^{1/2}/H$ (m s⁻¹) is the characteristic velocity used for the $\mathrm{Pr} > 1$ investigations [4,14,15]. Its use here will allow a direct comparison between the $\mathrm{Pr} > 1$ and $\mathrm{Pr} < 1$ results, in nondimensional form, as will be discussed in Sec. IV.

The appropriate initial and boundary conditions are

$$u = v = 0, \quad \theta = 0 \quad \text{at all } r,z \text{ and } \tau < 0;$$

and

$$u = 0, \quad \frac{\partial v}{\partial r} = 0, \quad \frac{\partial \theta}{\partial r} = 0 \quad \text{at } r = 0, 0 \le r \le 1;$$

$$u = v = 0, \quad \theta = -1 \quad \text{at } r = A^{-1}, 0 \le z \le 1;$$

$$u = v = 0, \quad \frac{\partial \theta}{\partial z} = 0 \quad \text{at } 0 \le r \le A^{-1}, z = 0;$$

$$u = v = 0, \quad \frac{\partial \theta}{\partial z} = 0 \quad \text{at } 0 \le r \le A^{-1}, \quad z = 1, \quad \text{and } \tau \ge 0.$$

The scaling laws given in Sec. II can be made dimensionless using the characteristic length H, the characteristic velocity V_0, and the characteristic time H/V_0 as follows. During the start-up stage of the boundary-layer development, the scaling laws (5), (6), (15), and (16) can be written in dimensionless form as

$$\delta_T = \frac{\Delta_T}{H} \sim \mathrm{Ra}^{-1/4} \tau^{1/2}, \qquad (29)$$

$$v_m = \frac{V_m}{V_0} \sim \mathrm{Pr}\,\tau, \qquad (30)$$

$$Nu \sim \frac{R_0}{\Delta_T} \sim \frac{1}{A \delta_T} \sim \frac{1}{A} \mathrm{Ra}^{1/4} \tau^{-1/2}. \tag{31}$$

$$\overline{Nu} \sim \int_0^1 \frac{1}{A \delta_T} dz \sim \frac{1}{A} \mathrm{Ra}^{1/4} \tau^{-1/2}, \tag{32}$$

and at the steady-state stage of the boundary-layer development, the scaling laws (8)–(13) and (17) can be written in dimensionless forms as follows,

$$\tau_b = \frac{t_b}{(H/V_0)} \sim \left(\frac{1-z}{\mathrm{Pr}}\right)^{1/2}, \tag{33}$$

$$\tau_{b,m} = \frac{t_{b,m}}{(H/V_0)} \sim \left(\frac{1}{\mathrm{Pr}}\right)^{1/2}, \tag{34}$$

$$\delta_{T,b} = \frac{\Delta_{T,b}}{H} \sim \left(\frac{1-z}{\mathrm{PrRa}}\right)^{1/4}, \tag{35}$$

$$\delta_{v,b,1} = \frac{\Delta_{v,b,1}}{H} \sim \left(\frac{(1-z)\mathrm{Pr}}{\mathrm{Ra}}\right)^{1/4}, \tag{36}$$

$$\delta_{v,b,2} = \frac{\Delta_{v,b,2}}{H} \approx \delta_{T,b} \sim \left(\frac{1-z}{\mathrm{PrRa}}\right)^{1/4}, \tag{37}$$

$$v_{m,b} = \frac{V_{m,b}}{V_0} \sim [(1-z)\mathrm{Pr}]^{1/2}. \tag{38}$$

$$\mathrm{Nu}_b \sim \frac{1}{A \delta_{T,b}} \sim \frac{1}{A}\left(\frac{\mathrm{PrRa}}{1-z}\right)^{1/4}. \tag{39}$$

Equations (29)–(31) clearly show that during the start-up stage, the boundary-layer development on the vertical sidewalls is independent of z, however, as shown by (35), (38), and (39), the boundary-layer development and the heat transfer across the vertical sidewall become z dependent at the steady-state stage of the boundary-layer development.

The scaling law for the time for the full stratification of the fluid in the cylinder, that is Eq. (19), can also be made dimensionless as follows,

$$\tau_s = \frac{t_s}{(H/V_0)} \sim \frac{1}{A}\left(\frac{\mathrm{Ra}}{\mathrm{Pr}}\right)^{1/4}. \tag{40}$$

Similarly, the scaling law (22) for the cooling down time t_f can also be written in dimensionless form as follows,

$$\tau_f = \frac{t_f}{(H/V_0)} \sim \frac{1}{A}\left(\frac{\mathrm{Ra}}{\mathrm{Pr}}\right)^{1/4}. \tag{41}$$

and the decay of the average dimensionless fluid temperature $\theta_a(\tau)$, from Eqs. (23) and (24), becomes

$$\theta_a(\tau) = \exp\left[-C_f A\left(\frac{\mathrm{Pr}}{\mathrm{Ra}}\right)^{1/4}\tau\right] - 1, \tag{42}$$

where C_f (dimensionless) is a constant of proportionality which will be determined below by numerical results.

B. Numerical method

Detailed information about the numerical algorithm and numerical accuracy tests can be found in [15]. Only a brief introduction is presented here.

The equations are discretized on a nonstaggered mesh using finite volumes, with standard second-order central difference schemes used for the viscous, pressure gradient, and divergence terms. The QUICK third-order upwind scheme is used for the advective terms [26]. The second-order Adams-Bashforth scheme and Crank-Nicolson scheme are used for the time integration of the advective terms and the diffusive terms, respectively. To enforce the continuity, the pressure correction method is used to construct a Poisson's equation which is solved using the preconditioned GMRES method. Detailed descriptions of these schemes were given in [27] and the code has been widely used for the simulation of a range of buoyancy dominated flows (see, e.g., [9,28,29]).

Due to the large variation in length scales it is necessary to use a computational mesh that concentrates points in the boundary layer and is relatively coarse in the interior. In this study, the meshes used for all runs are constructed using a stretched grid, with nodes distributed symmetrically with respect to the half-width and half-height of the computational domain represented by Fig. 1(b). The basic mesh used for Runs 1–5 and 10–12 has 299×299 grid points and the nearest grid point is located 0.0001 from the domain boundaries. Subsequently, the mesh expands at a fixed rate of 4.01% up to $r=z=0.1$ in both r and z directions. After that, the mesh size expansion rate decreases at a rate of 10% until it reaches zero, resulting in a constant coarser mesh in the interior of the domain. The meshes for Runs 6–9 are constructed in a similar fashion, but with different mesh size expansion rates at z direction, that is, 3%, 2.6%, 6.1%, and 7.6% for Runs 6–9, resulting in 299×227, 299×299, 299×297, and 299×297 grid points, respectively.

C. Numerical validation and quantification of the scaling laws

1. Boundary-layer development stage

The numerical results showing the scaling laws at the steady-state stage of the boundary-layer development, i.e., Eqs. (18), (33), (35), (38), and (39), are presented in Figs. 4 and 5, where it is found that these direct numerical simulation results agree very well with the scaling laws for A, Ra, and Pr in the ranges of $1/3 \leq A \leq 3$, $10^6 \leq \mathrm{Ra} \leq 10^{10}$, and $0.01 \leq \mathrm{Pr} \leq 0.5$. As can be seen the results fall approximately onto a straight line in all cases, showing that the scaling laws are providing a good representation of the steady-state development of the boundary layer for these ranges of the control parameters. The numerically quantified forms of these scaling laws are as follows,

$$\tau_b = 2.395\left(\frac{1-z}{\mathrm{Pr}}\right)^{1/2}, \tag{43}$$

$$\delta_{T,b} = 4.845\left(\frac{1-z}{\mathrm{PrRa}}\right)^{1/4}, \tag{44}$$
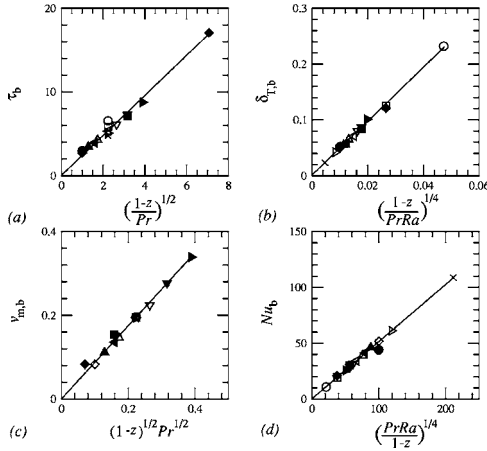
$$v_{m,b} = 0.872[(1-z)\mathrm{Pr}]^{1/2}, \tag{45}$$

FIG. 4. Numerical results for (a) τ_b plotted against $[(1-z)/\text{Pr}]^{1/2}$; (b) $\delta_{T,b}$ plotted against $[(1-z)/(\text{PrRa})]^{1/4}$; (c) $v_{m,b}$ plotted against $[(1-z)\text{Pr}]^{1/2}$; and (d) Nu_b plotted against $[\text{PrRa}/(1-z)]^{1/4}/A$. $\bigcirc$, Run1, $z=0.5$; $\square$, Run2, $z=0.5$; $\diamond$, Run3, $z=0.1$; $\triangle$, Run3, $z=0.3$; $\triangleleft$, Run3, $z=0.5$; $\triangledown$, Run3, $z=0.7$; $\triangleright$, Run4, $z=0.5$; $\times$, Run5, $z=0.5$; $\bullet$, Run6, $z=0.5$; $\blacksquare$, Run7, $z=0.5$; $\blacklozenge$, Run8, $z=0.5$; $\blacktriangle$, Run9, $z=0.167$; $\blacktriangleleft$, Run10, $z=0.253$; $\blacktriangledown$, Run11, $z=1.0$; $\blacktriangleright$, Run12, $z=1.515$; solid line, linear fit.

$$\text{Nu}_b = \frac{0.519}{A}\left(\frac{\text{PrRa}}{1-z}\right)^{1/4}, \tag{46}$$

$$\overline{\text{Nu}}_b = \frac{0.658}{A}(\text{PrRa})^{1/4}. \tag{47}$$

The numerical results for δ_T, v_m, Nu, and $\overline{\text{Nu}}$ at the start-up stage of the boundary-layer development are plotted as a ratio with respect to their steady-state values against the scaled times τ/τ_b and $\tau/\tau_{b,m}$ in Figs. 6 and 7, respectively. The results for $\tau/\tau_b < 1$ fall onto a straight line, showing the validity of scaling laws for the boundary-layer development at the start-up stage. For $\tau/\tau_b \geq 1$ the results fall onto a horizontal line, showing no time dependence, as is expected. The numerically quantified scaling laws are therefore as follows,
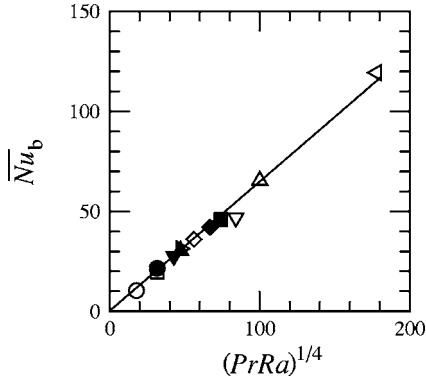

FIG. 5. Numerical results for $\overline{\text{Nu}}_b$ plotted against $(\text{PrRe})^{1/4}/A$. $\bigcirc$, Run1; $\square$, Run2; $\diamond$, Run3; $\triangle$, Run4; $\triangleleft$, Run5; $\triangledown$, Run6; $\triangleright$, Run7; $\bullet$, Run8; $\blacksquare$, Run9; $\blacklozenge$, Run10; $\blacktriangle$, Run11; $\blacktriangledown$, Run12. Solid line, linear fit.
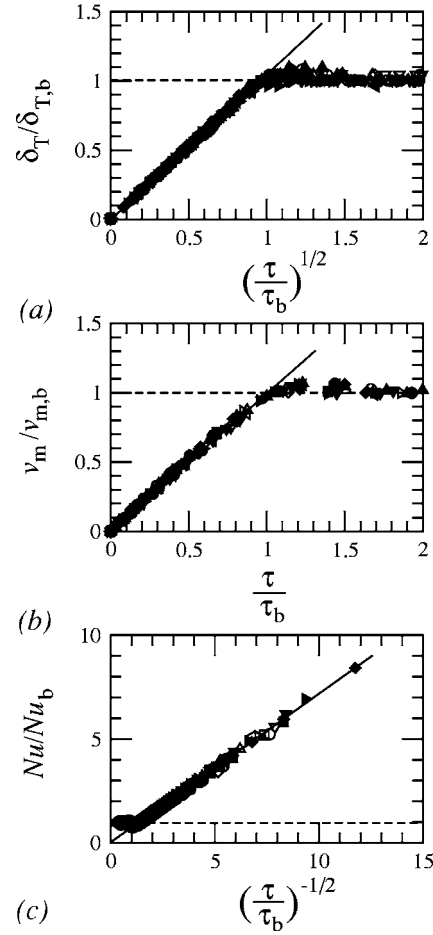

FIG. 6. Numerical results for (a) $\delta_T/\delta_{T,b}$ plotted against $(\tau/\tau_b)^{1/2}$; (b) $v_m/v_{m,b}$ plotted against τ/τ_b; and (c) Nu/Nu$_b$ plotted against $(\tau/\tau_b)^{-1/2}$. $\bigcirc$, Run1, $z=0.5$; $\square$, Run 2, $z=0.5$; $\diamond$, Run 3, $z=0.1$; $\triangle$, Run 3, $z=0.3$; $\triangleleft$, Run 3, $z=0.5$; $\triangledown$, Run 3, $z=0.7$; $\triangleright$, Run4, $z=0.5$; $\times$, Run5, $z=0.5$; $\bullet$, Run6, $z=0.5$; $\blacksquare$, Run7, $z=0.5$; $\blacklozenge$, Run8, $z=0.5$; $\blacktriangle$, Run9, $z=0.167$; $\blacktriangleleft$, Run10, $z=0.253$; $\blacktriangledown$, Run11, $z=1.0$; $\blacktriangleright$, Run12, $z=1.515$; solid line, linear fit for the start-up stage; dashed line, linear fit for the steady-state stage.

$$\frac{\delta_T}{\delta_{T,b}} = \left(\frac{\tau}{\tau_b}\right)^{1/2}, \tag{48}$$

$$\frac{v_m}{v_{m,b}} = \frac{\tau}{\tau_b}, \tag{49}$$

$$\frac{\text{Nu}}{\text{Nu}_b} = \left(\frac{\tau}{\tau_b}\right)^{-1/2}, \tag{50}$$

$$\frac{\overline{\text{Nu}}}{\overline{\text{Nu}}_b} = \left(\frac{\tau}{\tau_{b,m}}\right)^{-1/2}. \tag{51}$$

With the above relations (43)–(47), the numerical quantified scaling laws (48)–(51) for the boundary-layer development at the start-up stage can also be written as follows
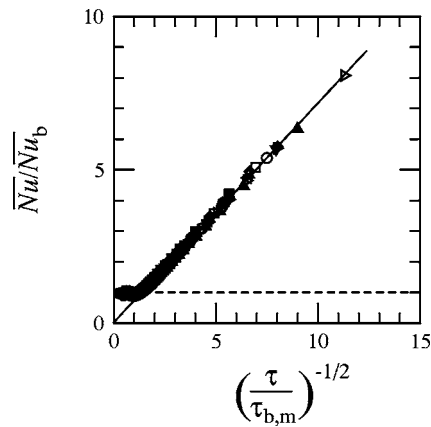
$$\delta_T = 3.131\text{Ra}^{-1/4}\tau^{1/2}, \tag{52}$$

FIG. 7. Numerical results for $\overline{\mathrm{Nu}}/\overline{\mathrm{Nu}}_b$ plotted against $(\tau/\tau_{b,m})^{-1/2}$. $\bigcirc$, Run1; $\square$, Run2; $\Diamond$, Run3; $\triangle$, Run4; $\triangleleft$, Run5; ∇, Run6; $\triangleright$, Run7; $\bullet$, Run8; $\blacksquare$, Run9; $\blacklozenge$, Run10; $\blacktriangle$, Run11; $\blacktriangledown$, Run12. Solid line, linear fit for the start-up stage; dashed line, linear fit for the steady-state stage.

$$v_m = 0.364 \mathrm{Pr}\, \tau, \tag{53}$$

$$\mathrm{Nu} = \frac{0.803}{A} \mathrm{Ra}^{1/4} \tau^{-1/2}, \tag{54}$$

$$\overline{\mathrm{Nu}} = \frac{1.018}{A} \mathrm{Ra}^{1/4} \tau^{-1/2}, \tag{55}$$

which clearly validate the scaling laws (29)–(32).

The Prandtl number scaling for the boundary-layer thicknesses at the steady state, i.e., Eqs. (35)–(37), is examined in detail by plotting the horizontal profiles of temperature and vertical velocity against $(1-r)\mathrm{Pr}^{1/4}$, as shown in Fig. 8 where both raw and scaled results are presented for a range of Pr. The scaling is seen to perform very well for the temperature profiles for $\mathrm{Pr} \leq 0.1$, with all profiles collapsing onto a single
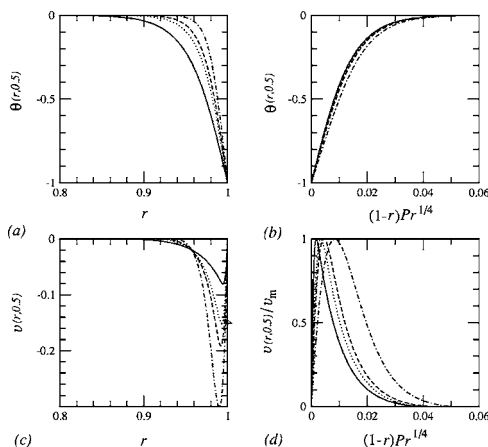

FIG. 8. Numerical results for the radial profiles of the temperature $\theta(r,0.5)$ and vertical velocity $v(r,0.5)$ at $z=0.5$ with different Pr: (a) $\theta(r,0.5)$ plotted against r; (b) $\theta(r,0.5)$ plotted against $(1-r)\mathrm{Pr}^{1/4}$; (c) $v(r,0.5)$ plotted against r; (d) $v(r,0.5)/v_m$ plotted against $(1-r)\mathrm{Pr}^{1/4}$ for $\mathrm{Ra}=10^8$ and $A=1$. ———, Pr $=0.01$; $\cdots$, Pr$=0.05$;$---$, Pr$=0.1$; and $-\cdot-$, Pr$=0.5$.
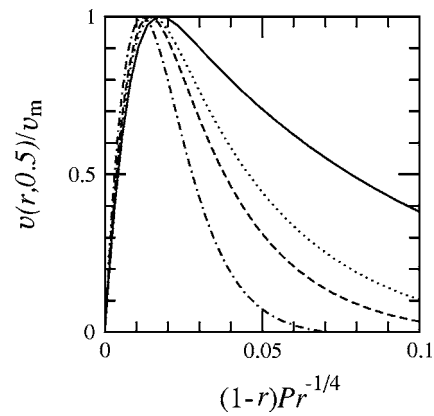

FIG. 9. Numerical results for the radial profiles of vertical velocity $v(r,0.5)/v_m$ at $z=0.5$ plotted against $(1-r)\mathrm{Pr}^{-1/4}$ with different Pr for $\mathrm{Ra}=10^8$ and $A=1$. ———, Pr$=0.01$; $\cdots$, Pr$=0.05$; $---$, Pr$=0.1$; and $-\cdot-$, Pr$=0.5$.

line. The Pr$=0.5$ result does not scale as well, indicating that the scaling law fails as Pr approaches 1.0, as is expected. This scaling is also seen to work well for Pr≤ 0.1 for the overall thickness of the viscous boundary layer, with all results having a scaled thickness of approximately 0.04, slightly less than that of the thermal boundary-layer thickness. Again the poor performance for Pr$=0.5$ is expected; however the scaling is also seen to work poorly in the large r, near-wall, region, with a large variation seen between all profiles in the scaled results. This indicates that the $\delta_{T,b}$ scaling is appropriate for $\delta_{v,b,2}$, but that it does not correctly represent the physics of the viscous boundary layer in the near wall region. The alternative scaling, $(1-r)\mathrm{Pr}^{-1/4}$, is also examined for the vertical velocity profiles, with the results shown in Fig. 9. This scaling is seen to perform better in the large r region bringing the maximum absolute velocity locations close together, however this scaling performs very poorly in the small r region. Apparently it is not possible to represent the behavior of the vertical velocity over δ_v with a single scaling. This is addressed below in Sec. IV.

2. Stratification stage

After the boundary layer achieves steady state the flow continues to develop via a stratification of the interior as a result of cooled fluid ejected from the boundary layer. The time scale τ_s for the development of full stratification, which is determined as the moment when the dimensionless average fluid temperature adjacent to the top boundary reaches -0.01, is plotted against $(\mathrm{Ra}/\mathrm{Pr})^{1/4}/A$, for a range of control parameters, in Fig. 10. The results all fall close to a straight line, confirming the validity of the scaling (40), with the full expression obtained by regression, as

$$\tau_s = \frac{0.313}{A} \left(\frac{\mathrm{Ra}}{\mathrm{Pr}}\right)^{1/4}. \tag{56}$$

3. Cooling-down stage

The temperature of the fluid in the cylinder will gradually approach that of the walls in the cooling-down stage. Theo-
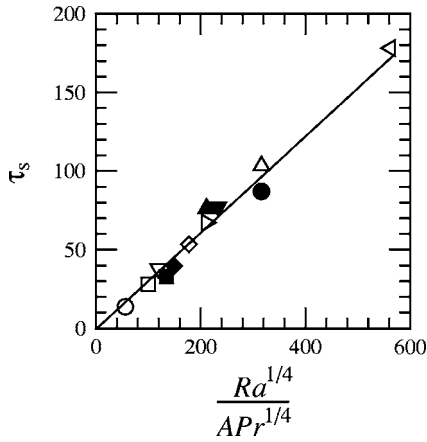
FIG. 10. τ_s plotted against $(Ra/Pr)^{1/4}/A$. $\bigcirc$, Run1; $\square$, Run2; $\diamond$, Run3; $\triangle$, Run4; $\triangleleft$, Run5; $\triangledown$, Run6; $\triangleright$, Run7; $\bullet$, Run8; $\blacksquare$, Run9; $\blacklozenge$, Run10; $\blacktriangle$, Run11; $\blacktriangledown$, Run12. Solid line, linear fit.

retically full cooling will only occur as time $\rightarrow \infty$. To obtain a finite cooling-down time it is necessary to arbitrarily define some percentage value, and we have chosen to use the 99 percentage. Therefore, the time for complete cooling τ_f was determined as the time at which $\theta_a(\tau_f) = -0.99$. The τ_f results are plotted against $(Ra/Pr)^{1/4}/A$ in Fig. 11 and show that this is an appropriate scaling for this phase of the flow. Linear regression gives the relation as

$$\tau_f = \frac{4.031}{A}\left(\frac{Ra}{Pr}\right)^{1/4}, \qquad (57)$$

which gives $C_f = 1.142$. Therefore, the full expression for the time decay of θ_a, Eq. (42), is obtained as

$$\theta_a(\tau) = \exp\left[-1.142A\left(\frac{Pr}{Ra}\right)^{1/4}\tau\right] - 1, \qquad (58)$$

which applies only for $\tau \leqslant \tau_f$ and with A, Ra, and Pr in the ranges of $1/3 \leqslant A \leqslant 3, 10^6 \leqslant Ra \leqslant 10^{10}$, and $0.01 \leqslant Pr \leqslant 0.5$.
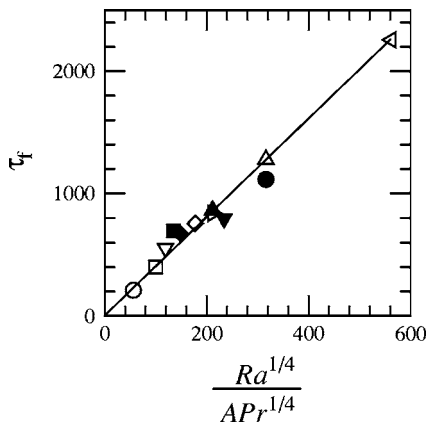

FIG. 11. τ_f plotted against $(Ra/Pr)^{1/4}/A$. $\bigcirc$, Run1; $\square$, Run2; $\diamond$, Run3; $\triangle$ Run4; $\triangleleft$, Run5; $\triangledown$, Run6; $\triangleright$, Run7; $\bullet$, Run8; $\blacksquare$, Run9; $\blacklozenge$, Run10; $\blacktriangle$, Run11; $\blacktriangledown$, Run12. Solid line, linear fit.
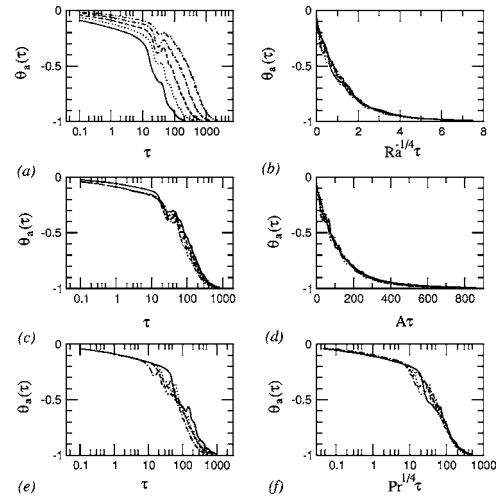

FIG. 12. Numerical results for (a) time series of $\theta_a(\tau)$ and (b) $\theta_a(\tau)$ plotted against $Ra^{-1/4}\tau$ for $Ra = 10^6$ (———), 10^7 ($\cdots$), 10^8 (– – –), 10^9 (–·–), and 10^{10} (–··–) with $A = 1$ and $Pr = 0.1$; (c) time series of $\theta_a(\tau)$ and (d) $\theta_a(\tau)$ plotted against $A\tau$ for $A = 1/3$ (———), $1/2$ ($\cdots$), 1 (– – –), 2(– · –), and 3 (–··–) with $Ra = 10^8$ and $Pr = 0.1$; (e) time series of $\theta_a(\tau)$; (f) $\theta_a(\tau)$ plotted against $Pr^{1/4}\tau$ for $Pr = 0.01$ (———), 0.05 ($\cdots$), 0.1 (– – –), and 0.5 (–··–) with $Ra = 10^8$ and $A = 1$, respectively.

Figure 12 contains the numerically obtained $\theta_a(\tau)$ for all 12 runs to show the dependence of the scaling law (42) on each individual control parameter Ra, A, and Pr. Figure 12(a) contains the raw data showing the time series of $\theta_a(\tau)$ for $Ra = 10^6$, 10^7, 10^8, 10^9, and 10^{10} with $A = 1$ and $Pr = 0.1$ unchanged. The scaling law (42) shows that the dependence of $\theta_a(\tau)$ on Ra goes like $Ra^{-1/4}$, and the time series of $\theta_a(\tau)$ with this scaling are shown in Fig. 12(b), where it is seen that this scale brings all five sets of data for different Ra together, indicating that $Ra^{-1/4}$ is the correct dependence of $\theta_a(\tau)$ on Ra in the scaling law (42). Similarly, Fig. 12(c) contains the raw data showing the time series of $\theta_a(\tau)$ for $A = 1/3$, $1/2$, 1, 2, and 3 with $Ra = 10^8$ and $Pr = 0.1$ unchanged. The scaling law (42) shows that the dependence of $\theta_a(\tau)$ on A goes like A, and the time series of $\theta_a(\tau)$ with this scaling are shown in Fig. 12(d), where, again, it is seen that this scale brings all five sets of data for different A together, indicating that A is the correct dependence of $\theta_a(\tau)$ on A in the scaling law (42). Figure 12(e) contains the raw data showing the time series of $\theta_a(\tau)$ for $Pr = 0.01$, 0.05, 0.1, and 0.5 with $Ra = 10^8$ and $A = 1$ unchanged. The scaling law (42) shows that the dependence of $\theta_a(\tau)$ on Pr goes like $Pr^{1/4}$, and the time series of $\theta_a(\tau)$ with this scaling are shown in Fig. 12(f), where the overlaying of all four sets of data for different Pr clearly shows that $Pr^{1/4}$ is the correct dependence of $\theta_a(\tau)$ on Pr in the scaling law (42).

The numerically obtained $\theta_a(\tau)$ is plotted against $A(Pr/Ra)^{1/4}\tau$ in Fig. 13(a) for all runs. The collapse of all sets of data onto a single curve again confirms that the scaling law (42) is true. The scaling for the full development of the average temperature is Eq. (58). This scaling is examined again by plotting the results for the time development of θ_a against $\exp[-1.142A(Pr/Ra)^{1/4}\tau]$ for all runs, as shown in
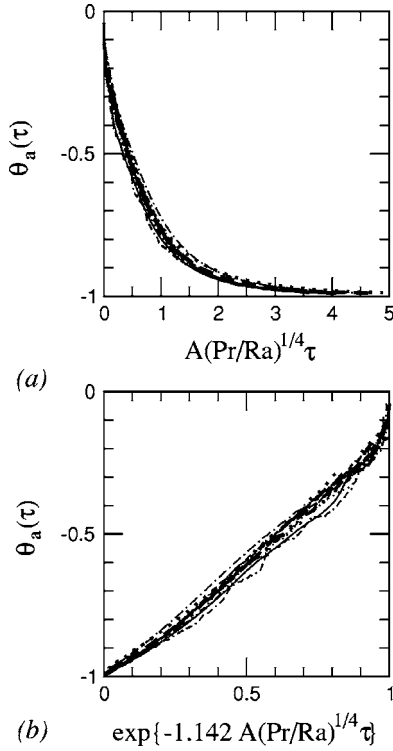
(a)

(b)

FIG. 13. Numerical results for $\theta_a(\tau)$ plotted against (a) $A(\mathrm{Pr}/\mathrm{Ra})^{1/4}\tau$ and (b) $e^{-1.142A(\mathrm{Pr}/\mathrm{Ra})^{1/4}\tau}$ for all simulation runs. ———, Run 1; $\cdots$, Run 2; – – –, Run 3 ;— — —, Run 4; – · – · –, Run 5; — · — · —, Run 6; ·– ·– ·–, Run 7; – – · – – · – –, Run 8; $\cdots$, Run 9; – – –, Run 10; – · – · –, Run 11; –· ·– ·–, Run 12.

Fig. 13(b). There is seen to be some variation in the scaled development, however it is seen Eq. (58) provides a good description of the overall development of θ_a.

The numerical results showing the dependence of the average Nusselt numbers on individual Ra, A, and Pr are presented in Fig. 14, where $\overline{\mathrm{Nu}}_a$ is the time average Nusselt number on the sidewall over τ_f, that is,

$$\overline{\mathrm{Nu}}_a = \frac{1}{\tau_f}\int_0^{\tau_f} \overline{\mathrm{Nu}}(\tau)d\tau. \qquad (59)$$

The time shown is scaled against τ_f, while the $\overline{\mathrm{Nu}}$ shown in (a), (c), and (e) are scaled with $\mathrm{Ra}^{1/4}$, A^{-1}, and $\mathrm{Pr}^{1/4}$ respectively. It is apparent that the time scaling combined with the Ra, A, and Pr scalings provides a good representation of the behavior of $\overline{\mathrm{Nu}}$, with all results collapsing close to single lines in (a), (c), and (e). The time-averaged results, shown in (b), (d), and (f), further confirm the $\overline{\mathrm{Nu}}$ scaling (18), showing very close to linear relations to $\mathrm{Ra}^{1/4}$, A^{-1}, and $\mathrm{Pr}^{1/4}$.

IV. DISCUSSIONS AND CONCLUSIONS

The cooling-down behavior of a fluid contained in a vertical cylinder subjected to isothermal boundary condition on the vertical walls is examined via scaling analysis and direct numerical simulation. Scaling laws have been obtained for the development time and properties of the initial vertical thermal boundary layer, of the stratification time, and of the
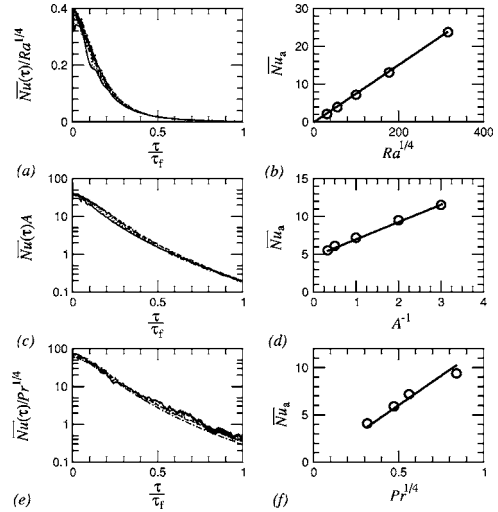

FIG. 14. Numerical results for (a) $\overline{\mathrm{Nu}}(\tau)\mathrm{Ra}^{-1/4}$ plotted against τ/τ_f and (b) $\overline{\mathrm{Nu}}_a$ plotted against $\mathrm{Ra}^{1/4}$ for $\mathrm{Ra}=10^6$ (———), 10^7 ($\cdots$), 10^8 (– – –), 10^9 (– · –), and 10^{10} (–· ·–) with $A=1$ and $\mathrm{Pr}=0.1$; (c) $\overline{\mathrm{Nu}}(\tau)A$ plotted against τ/τ_f and (d) $\overline{\mathrm{Nu}}_a$ plotted against A^{-1} for $A=1/3$ (———), $1/2$ ($\cdots$), 1 (– – – –), 2 (–·–), and 3 (–· ·–) with $\mathrm{Ra}=10^8$ and $\mathrm{Pr}=0.1$; (e) $\overline{\mathrm{Nu}}(\tau)\mathrm{Pr}^{-1/4}$ plotted against τ/τ_f and (f) $\overline{\mathrm{Nu}}_a$ plotted against $\mathrm{Pr}^{1/4}$ for $\mathrm{Pr}=0.01$ (———), 0.05 ($\cdots$), 0.1 (– – –), and 0.5 (–·–) with $\mathrm{Ra}=10^8$ and $A=1$.

full cooling-down time. The scalings have been obtained for $\mathrm{Pr}<1$, yielding different relations from those obtained for $\mathrm{Pr}>1$. For instance the scaling laws for the time development of the boundary layer, stratification, and full cooling-down stages are $\tau_b \sim (1-z)^{1/2}\mathrm{Pr}^{-1/2}$, $\tau_s \sim \mathrm{Ra}^{1/4}\mathrm{Pr}^{-1/4}/A$, and $\tau_f \sim \mathrm{Ra}^{1/4}\mathrm{Pr}^{-1/4}/A$, respectively, for $\mathrm{Pr}<1$, and $\tau_b \sim (1-z)^{1/2}$, $\tau_s \sim \mathrm{Ra}^{1/4}/A$, and $\tau_f \sim \mathrm{Ra}^{1/4}/A$, respectively, for $\mathrm{Pr}>1$ [14]. It is seen that for $\mathrm{Pr}>1$ the scaled quantities are independent of Pr, while for $\mathrm{Pr}<1$ they show a Pr dependency.

The numerical results have confirmed the scaling laws, providing scaling constants as well as illustrating the overall flow development. The only exception to the conclusive results is that of the vertical velocity boundary layer. The results presented in Fig. 8 show that the total vertical velocity boundary layer thickness has the same scaling as that of the thermal boundary layer thickness, however this scaling performs poorly in the near-wall region. In that region the alternative scaling, $(1-r)\mathrm{Pr}^{-1/4}$, provides better results. The $(1-r)\mathrm{Pr}^{-1/4}$ scaling is obtained by assuming that buoyancy balances horizontal diffusion of vertical velocity in the vertical velocity equation, which gives a velocity boundary layer thickness that scales with $\delta_{T,b}\mathrm{Pr}^{1/2}$, which is the same scaling as that obtained for this quantity for $\mathrm{Pr}>1$. However, for $\mathrm{Pr}<1$ this balance will only exist in the near-wall region, where $\partial^2 v/\partial r^2$ is positive; in the outer region the flow is being driven upwards via viscous effects and buoyancy. These quantities have the same sign and a balance will exist between them and inertia, providing a different scaling. It is therefore not possible to obtain a single scaling for the velocity structure over the full velocity boundary layer width. Nonetheless it is clear that for $\mathrm{Pr}<1$ the outer velocity boundary layer thickness has the same scaling and approxi-

mately the same magnitude as the thermal boundary layer thickness, supporting the statement of Gebhart *et al.* [21].

It was demonstrated in Ref. [14] that in a rectangular container with a $\text{Pr} > 1$ fluid, $\tau_{f,w}$ has the following scaling with A and Ra_w,

$$\tau_{f,w} \sim (A\text{Ra}_w)^{1/4},$$

where $\text{Ra}_w = g\beta(T_0 - T_w)W^3/(\nu\kappa) = \text{Ra}/A^3$ is the Rayleigh number defined by using the half-width (W) of the container as the characteristic length, and $\tau_{f,w}$ is the time scale made dimensionless by the characteristic time $W^2/\kappa\text{Ra}_w^{1/2}$. If H and $H^2/\kappa\text{Ra}^{1/2}$ are used as the characteristic length and time, as used in the current paper, the above scaling becomes

$$\tau_f \sim \frac{\text{Ra}^{1/4}}{A}.$$

Comparing it with Eq. (41), it is found that for both a $\text{Pr} > 1$ fluid and a $\text{Pr} < 1$ fluid, no matter whether it is in a vertical cylinder or in a rectangular container, τ_f is proportional to $\text{Ra}^{1/4}/A$. However, there is additional dependence of τ_f on Pr, that is $\tau_f \sim \text{Pr}^{-1/4}$ for a $\text{Pr} < 1$ fluid as shown in Eq. (41), whereas for a $\text{Pr} > 1$ fluid there is no dependence of τ_f on Pr. Nevertheless, it should be noted that for extreme values of A, that is for $A \gg 1$ (very tall container) or for $A \ll 1$ (very shallow container), the scalings may be quite different from those obtained in the current paper and in Ref. [14] where only intermediate values of A ($1/3 \leq A \leq 3$) are considered. Such extreme values of A are beyond the scope of the current paper.

[1] I. Catton, in *Proceedings of the 6th International Heat Transfer Conference*, edited by U. Grigull *et al.* (Hemisphere, Washington, 1978), Vol. 6, pp. 13–43; S. Ostrach, in *Proceedings of the 7th International Heat Transfer Conference*, edited by U. Grigull *et al.* (Hemisphere, Washington, 1982), Vol. 1, pp. 365–379; B. Gebhart *et al.*, *Buoyancy-Induced Flows and Transport* (Hemisphere, New York, 1988); J. M. Hyun, Adv. Heat Transfer **24**, 277 (1994); A. Bejan, *Convection Heat Transfer*, 2nd ed. (John Wiley & Sons, New York, 1995).

[2] R. J. Goldstein *et al.*, Int. J. Heat Mass Transfer **46**, 1887 (2003).

[3] G. I. Barenblatt, *Scaling, Self-similarity, and Intermediate Asymptotics* (Cambridge University Press, New York, 1996).

[4] J. C. Patterson and J. Imberger, J. Fluid Mech. **100**, 65 (1980).

[5] J. M. Hyun, Int. J. Heat Mass Transfer **27**, 1936 (1984); J. Heat Transfer **107**, 982 (1985).

[6] V. F. Nicolette and K. T. Yang, Int. J. Heat Mass Transfer **28**, 1721 (1985).

[7] D. R. Otis and J. Roessler, Int. J. Heat Mass Transfer **30**, 1633 (1987).

[8] S. G. Schladow, J. C. Patterson, and R. L. Street, J. Fluid Mech. **200**, 121 (1989).

[9] J. C. Patterson and S. W. Armfield, J. Fluid Mech. **219**, 469 (1990).

[10] S. W. Armfield and J. C. Patterson, Int. J. Heat Mass Transfer **34**, 929 (1991); S. W. Armfield and J. C. Patterson, J. Fluid Mech. **239**, 195 (1992); S. W. Armfield and R. Janssen, Int. J. Heat Fluid Flow **17**, 539 (1996).

[11] S. Xin and P. Le Quéré, J. Fluid Mech. **304**, 87 (1995).

[12] A. M. H. Brooker, J. C Patterson, and S. W. Armfield, J. Fluid Mech. **352**, 265 (1997).

[13] C. Lei and J. C. Patterson, J. Fluid Mech. **460**, 181 (2002).

[14] W. Lin and S. W. Armfield, Int. J. Heat Mass Transfer **42**, 4117 (1999); Int. J. Heat Fluid Flow **22**, 72 (2001); Phys. Rev. E **69**, 056315 (2004); , Int. J. Heat Mass Transfer **48**, 53

(2005).

[15] W. Lin, Ph.D. dissertation, The University of Sydney, Sydney, 2000 (unpublished).

[16] W. Lin, S. W. Armfield, and P. L. Morgan, Int. J. Heat Mass Transfer **45**, 451 (2002).

[17] R. D. C. Oliveski, A. Krenzinger, and H. A. Vielmo, Int. J. Heat Mass Transfer **46**, 2015 (2003).

[18] H. S. Kwak, K. Kuwahara, and J. M. Hyun, Int. J. Heat Mass Transfer **41**, 323 (1998).

[19] F. P. Incropera and D. P. DeWitt, *Fundamentals of Heat and Mass Transfer*, 4th ed. (John Wiley & Sons, New York, 1996), p. 319.

[20] D. J. Tritton, *Physical Fluid Dynamics* (Oxford University Press, Oxford, 1995), p. 170.

[21] B. Gebhart *et al.*, *Buoyancy-Induced Flows and Transport* (Hemisphere, New York, 1988), p. 53.

[22] A. Bejan, *Heat Transfer* (John Wiley & Sons, Inc., 1993), p. 350; D. Henry and M. Buffat, J. Fluid Mech. **374**, 145 (1998); A. Yu. Gelfgat, P. Z. Bar-Yoseph, A. Sloan, and T. A. Kowalewski, Int. J. Trans. Phenomena **1**, 173 (1999); I. D. Piazza and M. Ciofalo, Int. J. Heat Mass Transfer **43**, 3027 (2000); A. Yu. Gelfgat, P. Z. Bar-Yoseph, and A. Sloan, J. Cryst. Growth **220**, 316 (2000); S. Arcidiacono, I. D. Piazza, and M. Ciofalo, Int. J. Heat Mass Transfer **44**, 537 (2001).

[23] A. Juel, T. Mullin, H. Ben Hadid, and D. Henry, J. Fluid Mech. **436**, 267 (2001).

[24] S. W. Armfield and G. D. McBain, in *Proceedings of the 15th Australasian Fluid Mechanics Conference*, edited by M. Behnia, W. Lin, and G. D. McBain (The University of Sydney, Sydney, 2004), paper AFMC00238.

[25] A. F. Mills, *Heat Transfer*, 2nd ed. (Prentice Hall, Upper Saddle River, 1999), p. 31.

[26] B. P. Leonard, Comput. Methods Appl. Mech. Eng. **19**, 59 (1979).

[27] S. W. Armfield, Comput. Fluids **20**, 1 (1991); S. W. Armfield

and R. L. Street, J. Comput. Phys. **153**, 660 (1999).

[28] S. W. Armfield and W. Debler, Int. J. Heat Mass Transfer **36**, 519 (1993); A. Javam, J. Imberger, and S. W. Armfield, J. Fluid Mech. **396**, 183 (1999).

[29] W. Lin and S. W. Armfield, Phys. Rev. E **66**, 066308 (2002); J. Fluid Mech. **403**, 67 (2000); Int. J. Heat Mass Transfer **43**, 3013 (2000); Comput. Mech. **31**, 379 (2003); Numer. Heat Transfer, Part A **38**, 377 (2000); Energy **23**, 719 (1998).